Energy & Environmental Science

Ballistic ion transport through hierarchically-ordered-structure polymer binder

Journal:	*Energy & Environmental Science*
Manuscript ID	EE-ART-12-2024-006071.R1
Article Type:	Paper
Date Submitted by the Author:	23-Mar-2025
Complete List of Authors:	Li, Defu; Lawrence Berkeley National Laboratory Chen, Fang; Lawrence Berkeley National Laboratory Thapa, Santosh; University of Kentucky Sternlicht, Hadas; Lawrence Berkeley National Laboratory Lee, Gi-Hyeok; Lawrence Berkeley National Laboratory, Advanced Light Source Ahmed, Faiz; Lawrence Berkeley National Laboratory Jin, Xiuyu; Lawrence Berkeley National Laboratory, Energy Storage & Distributed Resources Division Miao, Qiusu; University of California Berkeley Giovine, Raynald; University of California Berkeley Yang, Wanli; Lawrence Berkeley National Laboratory, Advanced Light Source Minor, Andrew; University of California Berkeley, Materials Science and Engineering Cheng, Yangtse; University of Kentucky Liu, Gao; Lawrence Berkeley National Laboratory

Broader context

All-solid-state batteries (ASSBs) have gained increasing research attention due to their enhanced safety and high energy density. However, poor ion transport within electrode materials, particularly polymer binders, continues to pose a challenge. Silicon has emerged as a promising candidate for anode material in ASSB due to its high theoretical capacity (~3700 mAh/g), low cost, and abundant availability. However, silicon experiences significant volume variation during lithiation/delithiation process. Incorporating polymer binder offers an effective method to accommodate volume variation of silicon and preserve structural integrity of electrode materials. Thus, a polymer binder with mixed electronic-ionic conductive (MEIC) property is highly demanded since it can effectively ensure good electrical and ionic contact with Si during battery cycling. One state-of-the-art method is to graft a polyethylene glycol (PEO) chain onto a conjugated backbone to achieve the MEIC property, but PEO exhibits low ion conductivity at room temperature. We present a ballistic ion transport mechanism within a MEIC polymer binder, achieving Li^+ conductivity one to two orders of magnitude higher than that of PEO. This mechanism enables the polymers to achieve both mechanical robustness and superior conductivity, which is inaccessible in polymers that rely on segmental motion to facilitate ion transport.

ARTICLE

Ballistic ion transport through hierarchically-ordered-structure polymer binder

Received 00th January 20xx,
Accepted 00th January 20xx

DOI: 10.1039/x0xx00000x

Defu Li[a], Chen Fang[a], Santosh Thapa[b], Hadas Sternlicht[c,d], Gi-Hyeok Lee[e], Faiz Ahmed[a], Xiuyu Jin[a], Qiusu Miao[a,f], Raynald Giovine[g], Wanli Yang[e], Andrew Minor[c,d], Yang-Tse Cheng[b,h], Gao Liu[a,*]

Since its discovery in the 1970s, solid-state ion conduction within polymers has primarily relied on polymer segmental motion to drive ion diffusion. However, ion transport based on polymer dynamics features low ionic conductivity (usually < 10^{-5} S/cm) at room temperature and highly depends on temperature, which influences performance by controlling the ratio of amorphous to crystalline composition in polymers. A faster ion transport mechanism, independent of polymer dynamics, has long been sought but remains inaccessible. Here, we report a ballistic ion transport mechanism in a mixed electronic-ionic conductive (MEIC) polymer binder, where its hierarchically ordered structure facilitates ion diffusion and achieves solid-state Li^+ conductivity in the range of 10^{-4} to 10^{-3} S/cm from -20 to 70 °C. This mechanically robust MEIC polymer is a versatile ionic conductor, allowing Li^+, Na^+, or K^+ to diffuse through polymer matrix, with their cationic charges counterbalanced by electrons on conjugated polymer backbones. Traditional polymer binders have typically been classified as inactive materials due to their negligible capacity. In contrast, this polymer binder features a high Li^+ ion capacity of nearly 1000 mAh/g, transforming it into an active material and providing a method to enhance energy density. This work establishes a foundation and inspires a design principle for engineering multifunctional polymer binders with superionic conductivity, high electronic conductivity, high capacity, and mechanical robustness, thereby extending their applications in the field of solid-state energy.

Broader context

All-solid-state batteries (ASSBs) have gained increasing research attention due to their enhanced safety and high energy density. However, poor ion transport within electrode materials, particularly polymer binders, continues to pose a challenge. Silicon has emerged as a promising candidate for anode material in ASSB due to its high theoretical capacity (~3700 mAh/g), low cost, and abundant availability. However, silicon experiences significant volume variation during lithiation/delithiation process. Incorporating polymer binder offers an effective method to accommodate volume variation of silicon and preserve structural integrity of electrode materials. Thus, a polymer binder with mixed electronic-ionic conductive (MEIC) property is highly demanded since it can effectively ensure good electrical and ionic contact with Si during battery cycling. One state-of-the-art method is to graft a polyethylene glycol (PEO) chain onto a conjugated backbone to achieve the MEIC property, but PEO exhibits low ion conductivity at room temperature. We present a ballistic ion transport mechanism within a MEIC polymer binder, achieving Li^+ conductivity one to two orders of magnitude higher than that of PEO. This mechanism enables the polymers to achieve both mechanical robustness and superior conductivity, which is inaccessible in polymers that rely on segmental motion to facilitate ion transport.

Introduction

Ballistic ion transport in polymers has been pursued over decades but remains unachievable utilizing conventional polymers with ion transport mechanism driven by segmental motion. The next-generation multifunctional polymer binders must fulfil traditional roles, providing mechanical adhesion and electronic conductivity, while also exhibiting superior ionic conductivity. Sluggish ion transport has consistently been a major bottleneck to the wide implementation of conductive polymer binders in battery applications, especially in the field of solid-state energy.

Ion transport within polymers has mainly depended on polymer dynamics to drive ion diffusion in a solid-state environment

[a] *Energy storage and Distributed Resources Division, Lawrence Berkeley National Laboratory, Berkeley, CA, USA. Email: gliu@lbl.gov*
[b] *Department of Physics and Astronomy, University of Kentucky, Lexington, KY, USA.*
[c] *National Center for Electron Microscopy, The Molecular Foundry, Lawrence Berkeley National Laboratory, Berkeley, CA, USA.*
[d] *Department of Materials Science and Engineering, University of California, Berkeley, CA, USA.*
[e] *Advanced Light Source, Lawrence Berkeley National Laboratory, Berkeley, CA, USA*
[f] *College of Chemistry, University of California, Berkeley, CA, USA.*
[g] *College of Chemistry Pines Magnetic Resonance Center - Core Facility, University of California, Berkeley, CA, USA*
[h] *Department of Chemical and Material engineering, University of Kentucky, Lexington, KY, USA.*
Supplementary Information available: [details of any supplementary information available should be included here]. See DOI: 10.1039/x0xx00000x

since Wright's discovery of ion transport in polyethylene glycol (PEO)-alkali salt complexes in the 1970s.[1, 2] Polymer is soft and pliable above its glass transition temperature (T_g) due to polymer segmental motion, whereas below T_g, the polymer segmental motion reduces to minimum, thus the polymer is glassy and hard. Ionic conductive polymers, such as PEO, feature moderate lithium ionic conductivity (σ^+) at temperatures above T_g.[3, 4] However, as the temperature drops below T_g. The σ^+ decreases by several orders of magnitude, and reduces to near zero. In addition, since partial crystallinity of the polymer restrains polymer segmental motion, the σ^+ of polymer can drastically decrease in the presence of crystalline domains. Therefore, the Arrhenius relationship between temperature and conductivity of a conventional polymer bends down at every phase transition of the polymer from polymer melt to partially crystalline states, and to glassy state.[3-5] Additionally, these polymers confront a trade-off between σ^+ and mechanical strength. Specifically, the softer the polymers, the higher the σ^+, and vice versa. Therefore, achieving high σ^+ at ambient to low temperatures faces tremendous challenges in a mechanically robust polymer host.

Vehicle transport mechanism in organic liquid electrolyte features superior σ^+ in the range of 10^{-2}-10^{-3} S/cm.[3] Solid polymer electrolytes, such as PEO with lithium salts, have an approximate σ^+ in the range of 10^{-8} to 10^{-5} S/cm at room temperature, inadequate for practical applications.[3, 6, 7] Polymer melt of PEO and lithium salts above melting temperature (~60 °C) possesses an approximate σ^+ of 10^{-5}-10^{-4} S/cm.[6, 8] Many polymer engineering and chemistry approaches have been explored to design and fabricate mixed electronic-ionic conductive (MEIC) polymers,[9] including mixing conjugated polymers with polyelectrolyte or polymer electrolyte blends,[10, 11] synthesis of block-copolymers with both electrical and ionic blocks,[12] and modification of conjugated polymer backbones by grafting ion-conducting side chains.[13, 14] Nevertheless, these polymers still encountered difficulty in achieving stable σ^+ exceeding 10^{-4} S/cm at ambient temperature in solid-state conditions.[3, 6, 7] Additionally, this design strategy, which integrates electronically and ionically conductive components, faces a tradeoff between ionic and electrical conductivities due to opposing transport mechanisms. Electroconductive polymers with conjugate backbones preferred highly ordered, packed, and well-aligned chains to form a high degree of π-π stacking structures. These rich π-π stacking regions facilitate interchain electron transport and ultimately contribute to superior electronic conduction over macroscopic range. However, the rigid polymer structures prevent ion dissociation and significantly suppress ion transport that replies on chains flexibility and dynamics. Therefore, current approaches encounter difficulty in simultaneously enhancing both electronic and ionic conductivity. Additionally, soft polymers feature low mechanical strength, whereas many electrochemical devices require high mechanical strength.

Here, we report a long-range and fast ballistic ion transport mechanism within an electronically conductive and mechanically robust polymer binder, independent of polymer segmental motion (Note S1). In this system, cationic ions (Li^+, Na^+, or K^+) diffuse through hierarchically ordered structure (HOS) polymer matrix with electrons as the only counter charges, while the polymer is in a glassy and structurally robust state. This class of MEIC polymer is desirable as they not only preserve the unique attributes of polymers, such as design flexibility, functional versatility, and easy processability, but also possess excellent ionic and electronic conductivity. For this ballistic ion transport mechanism, not controlled by solvation and chain segmental motion, a single Arrhenius relationship exists for the ionic conductivity across a wide range of operating temperature regardless of polymer phase transitions, contributing to their superior σ^+ at low temperatures. The MEIC polymers find potential applications in organic electronics[15, 16], energy conversion, optoelectronic thin film devices, and electrochemical thin film devices,[9, 16] which demand elevated ion-doping levels and fast ion mobility. Their MEIC advantages position them as promising polymer binders for high-energy-density all-solid-state batteries (ASSBs), as well as the potential utility for Na- or K-based energy storage devices. Additionally, their solvent processability offers opportunities for industry-scale fabrication processes.

Results and Discussion

Results and Discussion

Polymer engineering to achieve ballistic ion transport

Conjugated polymers such as polyacetylene and polyphenylene encounter challenges in solution and melt processing due to poor solubility and high T_g, which hinder their broad applications. To overcome these challenges, a two-step method was harnessed to engineer HOS polymers with MEIC features. First, poly(9,9-dioctylfluorene-co-fluorenone-comethylbenzoicester) PFM polymers was synthesized to enhance solubility and processability by including flexible and long alkyl side chains (Fig. 1a(i)).[17, 18] Second, the PFM polymer is thermal processed at 500 °C to cleave the alkyl side chains and $-CH_3$ group in ester side chains but retains the more stable conjugated polymer backbone and functionalities.[19] Despite their advantages in solvent solubility, the long and flexible alkyl side chains of PFM occupied large space, disrupted conjugated polymer backbone alignments, suppressed π-π stacking formation, and hindered Li^+ doping and transport, as represented in Fig. 1b[19]. Without the alkyl side chains, HOS-PFM possessed highly packed, ordered, and well aligned conjugated backbones in the scale of tens of nanometers, contributing to a higher degree of π-π stacking and formation of nanocrystalline morphology (Fig. 1c; Fig. S1). These extended π-π stacking regions significantly facilitated interchain electron transport, contributing to electronic conductivity of HOS-PFM three orders of magnitudes higher than that of PFM at undoped states and five orders of magnitudes higher at doped states.[19] The HOS-PFM featured the capacity to store Li^+ and possessed nearly 1000 mAh/g Li^+ capacity at the highest doped state (Table S1,S2; Fig. S2,S3; Note S2) while the PFM polymer has none (Fig. S4; Note S3). Elevated doped Li^+ content within the HOS-PFM structure enhanced electronic conductivity by 2-3 orders of

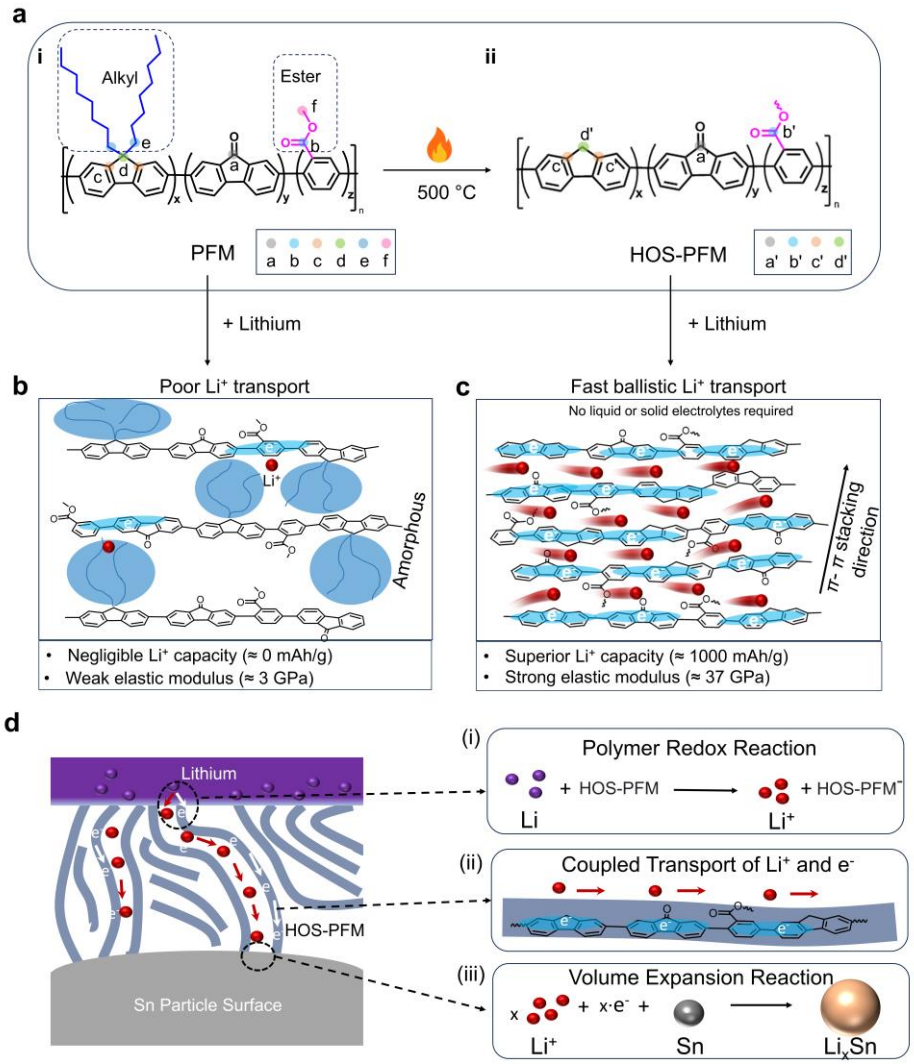

Fig. 1 Molecular structure and schematic demonstration. (a) Transformation of (i) PFM to (ii) HOS-PFM via thermal treatment at 500 °C. (b,c) Schematics of Li^+ doping and transport within (b) PFM and (c) HOS-PFM. (d) Schematics of (i) polymer redox reaction between Li and HOS-PFM, (ii) ballistic Li^+ transport within HOS-PFM polymer matrix, counterbalanced by electrons on the conjugated backbone, and (iii) Li^+ and Sn reaction, accompanied by ~300% volume expansion.

magnitude.[19] In ballistic transport, electron and ions exhibited coupling and concurrent transport behaviors (Fig. 1c), contributing to synergistic effect. Therefore, higher Li^+ capacity led to higher electronic conductivity, which subsequently facilitated fast Li^+ movement.

Tailored experiments to illustrate ballistic ion transport

To validate the ballistic Li^+ transport over a micrometer-scale distance, two tailored-designed double-layered electrodes (DLEs) were engineered, each comprising an upper and lower layer (Fig. 1d and Fig. S5). The lower layer contained a mixed composite of Sn nanoparticles and HOS-PFM polymers. The upper layer consisted of either PFM (Fig. S6) or HOS-PFM (Fig. S7) content, denoted as PFM/Sn DLE or HOS-PFM/Sn DLE, respectively. The objective was to verify whether alkali ions (Li^+, Na^+, and K^+) could diffuse through a 2-4 μm thick PFM or HOS-PFM layer to undergo a reaction with crystalline Sn particles. Initially, Li metal was compressed against the PFM/Sn DLEs or HOS-PFM/Sn DLEs to trigger a polymer redox reaction driven by potential difference between Li metal and the polymers (Fig. 1d). During this process, Li metal experienced electron loss and oxidation reaction, while the HOS-PFM polymers underwent electron absorption and reduction reaction. Concurrently, Li^+ diffused into the polymer matrix. Meanwhile, the electrons were stabilized by the polymers and migrated via conjugated backbone, counterbalanced by Li^+. After traveling through the HOS-PFM layer, these Li^+ and electrons eventually reached Sn's nanoparticle surface and triggered an alloy reaction between Li^+ and Sn (Fig. 1d).

Polymer functionality preservation during pyrolytic conversion

Polymers structures prior to and after the thermal treatment were analyzed using solid-state NMR (ssNMR). Initially, an analysis of the ^1H ssNMR spectra reveals that the PFM structure comprises 8 distinct ^1H environments within the alkyl side chains, each corresponding to unique chemical shifts, and 9

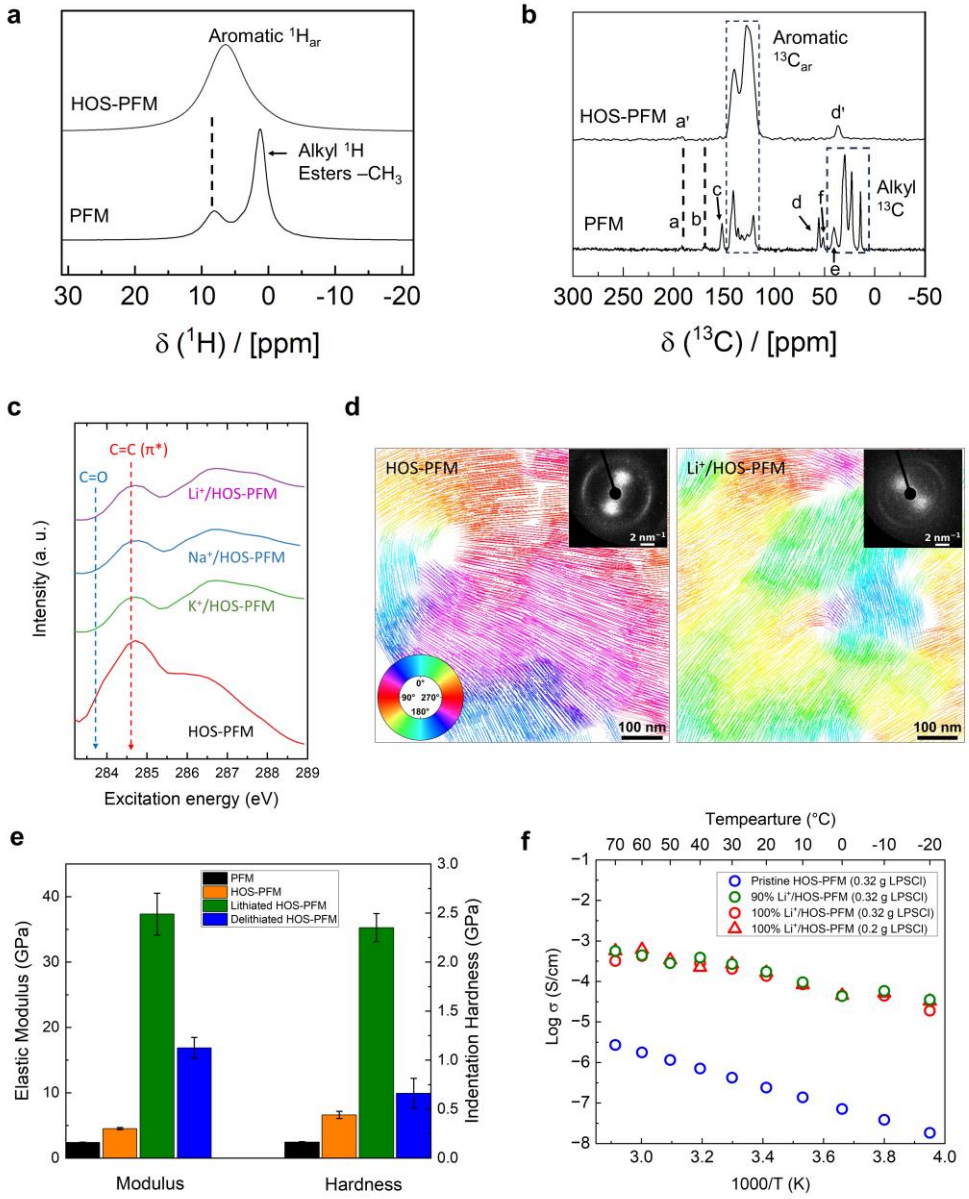

Fig. 2 Transformation from PFM and properties of the conductive HOS-PFM. (a,b) (a) ^{1}H spin-echo and **(b)** ^{1}H→^{13}C CPMAS ssNMR spectra. Specific ^{13}C NMR signals in PFM and HOS-PFM are indexed as (a) to (f) or (a') to (d'), respectively and their corresponding carbon are indicated in the molecular structures of PFM and HOS-PFM in Fig. 1a. (c) sXAS characterization of pristine HOS-PFM and the HOS-PFM samples doped with Li^+, Na^+, or K^+. (d) Flow line maps tracking the backbones and diffraction patterns (insets, weighted averages over 3×3 pixels) of pristine HOS-PFM and Li^+/HOS-PFM polymers via 4D STEM. The color wheel represents the orientation of the backbone chains. (e) Elastic modulus and indentation hardness. (f) Continuous Arrhenius relationship across a wide temperature window.

distinct ^{1}H environments within the PFM backbone. In contrast, the HOS-PFM structure is expected to exhibit only backbone signals, as the thermal treatment eliminates the side chains. This suggests that PFM exhibits a broad distribution of ^{1}H environments in the regions of aromatic protons (H_{ar}) and alkyl protons (H_{al}), whereas HOS-PFM will present only H_{ar} signals.

^{1}H resolution tends to be limited in ssNMR at moderate MAS frequencies, compared to solution-state NMR. This limitation arises primarily from strong homonuclear ^{1}H-^{1}H dipolar coupling and chemical shift distribution (or dispersion) caused by disorder in the sample, which affect ^{1}H line shape and broaden individual signals.[20-22] For PFM and HOS-PFM, the combination of the many ^{1}H environments with close chemical shifts (expected in the H_{ar} and H_{al} regions) and the broadening of individual signals (due to ^{1}H-^{1}H dipolar coupling) is expected to lead to significant signal overlaps, resulting in a broad ^{1}H line shape with limited resolution. On the other hand, dynamic motion such as fast rotation of terminal groups or side chain rotation can partially average ^{1}H-^{1}H homonuclear dipolar coupling, thereby reducing ^{1}H broadening in the H_{al} region.[20, 23]

Quantitative ssNMR ^{1}H spin-echo spectra of PFM and HOS-PFM were shown in Fig. 2a. The PFM features two main resonances centered around 8 and 1.3 ppm, the latter being much sharper and more intense with a nearly 1:3 ratio after integration. The signal at 8 ppm was attributed to the aromatic proton (H_{ar}) in the polymer backbone, while the sharper and more intense signal around 1.3 ppm corresponded to the aliphatic protons (H_{al}) in the alkyl sidechain and terminal methyl groups of 9,9-dioctylfluorene and methylbenzoic ester monomers, respectively. Conversely, the HOS-PFM exhibited a single broader resonance compared to PFM and centered around 6.5 ppm. The observed chemical shift agrees with a polymer structure containing aromatic protons while the slight broadening and featureless ^{1}H line shape suggest a more pronounced distribution of ^{1}H environments.[20] The $^1H_{ar}$ signals were observed for both PFM (8 ppm) and HOS-PFM (6.5 ppm), indicating that these H_{ar} sites were conserved upon heat treatment and only the H_{al} (1.3 ppm) were lost.

The observed ^{13}C signal split into two main groups. The ^{13}C signals ranging from 0 to 60 ppm were attributed to non-aromatic carbons, while the signals from 100 to 200 ppm were typical of carbon with an aromatic character. In PFM (Fig. 2b), the ^{13}C peaks observed from 14.4 ppm to 40.6 ppm correspond to the eight different carbon atoms in the alkyl side chains, while the many overlapping ^{13}C signals observed from 115 ppm to 148 ppm correspond to the aromatic carbon that forms the PFM polymer backbone. Compared to that of PFM, the ^{13}C spectrum of HOS-PFM underwent significant changes due to loss of the long alkyl side chains and terminal methyl groups of methylbenzoic ester units during thermal processing. The most intense ^{13}C signals overlap from 100 to 160 ppm, typical of aromatic carbons (C_{ar}) within the polymer backbone, were retained. However, the most intense signals observed in PFM in the 0 to 60 ppm region vanished. Detailed discussion regarding site a to f and a' to f' (Fig. 1a,2b) are included in Note S4. The resultant HOS-PFM maintained polymer nature and distinguished itself from carbon materials.

Elevated electronic conductivity

Fig. 2c illustrated the C *K*-edge soft X-ray absorption spectroscopy (sXAS) spectra in partial fluorescence yield (PFY) extracted from high-efficiency RIXS maps (Fig. S8,S9) of the HOS-PFM and its alkali ion-doped derivatives. Prior research has found that the carbonyl group of PFM introduced a lowest unoccupied molecular orbital (LUMO) positioned at a lower energy level compare to the typical low-energy orbital from C=C π* in conjugated polymers[17], indicated by the lowest energy shoulder of HOS-PFM (blue dashed arrow). This low energy state decreased the band gap and improved overall electric conductivity, consistent with previous reports.[17, 19] After doping with Li^+, Na^+, or K^+, electrons filled in these low energy states, leading to their disappearance in all the doped samples. More significantly, the spectral peak corresponding to the C=C π* state was heavily suppressed compared with the high energy features around 286-288 eV (Fig. 2c). This indicated that the electrons were not only doped into the aforementioned LUMO states, but also doped directly into the C=C π* framework. This intrinsic attribute of HOS-PFM presented the potential to facilitate electron migration and further enhance electronic conductivity.

Robust structure upon Li^+ intercalation

Four-dimensional scanning transmission electron microscopy (4D STEM) was utilized to reveal the degree of the polymer arrangement before and after doping Li^+, which is associated with oriented π–π stacking between the polymer chains. Using 4D STEM, we discerned between rotationally homogenous rings and low-q oriented pairs of lobes, associated with amorphous PFM and HOS-PFM, respectively. After thermal processing at 500 °C, the resultant polymer exhibited HOS feature, and the polymer chain alignment orientation was depicted in Fig. 2d, similar as a previous study[19]. These HOS, which exhibited ordered and rich π-π stacking, reinforced interchain charge transport, thereby achieving macroscopic electronic conduction. After doping with Li^+, the Li^+/HOS-PFM polymer retained the HOS feature, indicating initial stability to Li^+ intercalation during a single lithiation event. This retention of HOS attribute facilitates stable pathways for macroscopic electron migration as well as fast Li^+ transport within the polymer matrix.

Robust and reversible mechanical properties

Mechanical properties of polymer binder play a critical role in battery performance since the polymer must preserve electrode integrity and accommodate volumetric changes in the active materials. The nanoindentation results showed that the HOS-PFM exhibited an 87.6% higher elastic modulus and a 171% higher hardness compared to the PFM (Fig. 2e). Furthermore, the PFM featured large plastic deformation behavior while the HOS-PFM exhibited significant elastic recovery or rubber-like deformation attributes after unloading (Fig. S10). The PFM possessed flexible alkyl side chains, which softened structures and led to plasticization effect. After thermal removal of the alkyl side chains, the HOS-PFM featured densely stacked and well-defined polymer structures, acting as resilient leaf springs for elastic recovery. No significant variations are observed in the load-displacement profiles, elastic modulus, and hardness between pristine PFM, lithiated PFM, and delithiated PFM samples (Fig. S10, S11; Note S5). The negligible Li^+ ion capacity of the PFM polymers results in nearly unchanged mechanical properties after lithiation or delithiation. In comparison, after doping Li^+, the elastic modulus and hardness of lithiated HOS-PFM increased by approximately 725% and 433%, respectively, compared to the HOS-PFM (Fig. 2e; Fig. S11). These significant enhancements were likely caused by the ionic interactions between inserted Li^+ ions and polymer chains (Note S6). The negatively charged electrons along the conjugated backbone chains can form electrostatic interactions with the positively charged Li^+ ions. When a lithium ion dynamically interacts with two or more adjacent negatively charged polymer chains, it can potentially serve as a reversible and dynamic ionic cross-link between polymer chains. After removing the inserted Li^+ ions, the elastic modulus and hardness of delithiated HOS-PFM noticeably decreased but remained higher than those of the

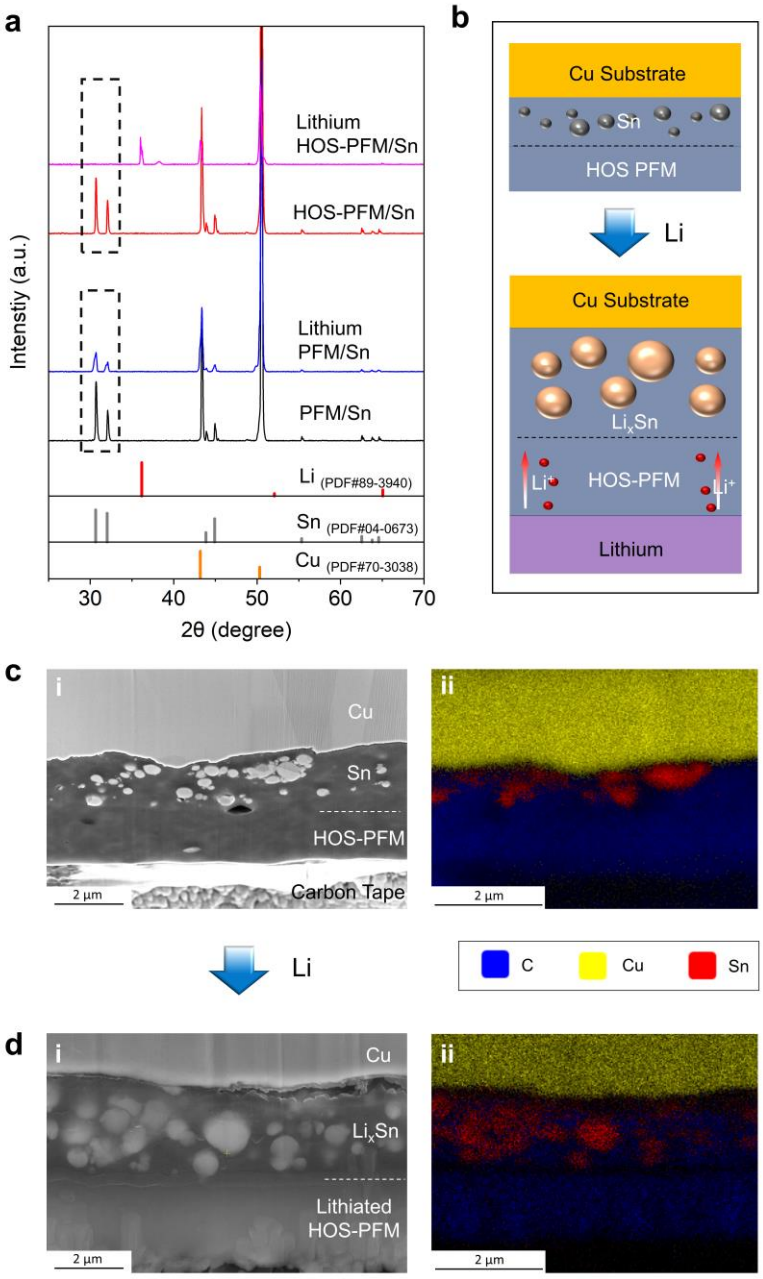

Fig. 3 Demonstration of long-range ballistic Li^+ transport. (a) XRD patterns. Crystalline peaks loss of Sn reflected that Li^+ diffused through effectively in HOS-PFM but not PFM. (b) Illustration of morphological evolution of Sn within HOS-PFM/Sn DLEs after Li^+ traversed HOS-PFM layer and reacted with Sn. (c,d) FIB cross-sections of HOS-PFM/Sn DLEs (c) before and (d) after compression of Li metal. Volume expansion of Sn particles confirmed that Li^+ passed though HOS-PFM layer. The crystalline and morphological evolution of Sn particles validated that Li^+ ion passed through the HOS-PFM layer.

HOS-PFM (Fig. 2e; Fig. S11; Note S5). This phenomenon occurred primarily caused by incomplete de-lithiation of Li^+ within the HOS-PFM matrix. The partial recovery in elastic modulus and hardness indicated that the changes in mechanical properties were associated with the Li^+ content in the polymers. During lithiation, the enhanced elastic modulus and hardness of HOS-PFM could control and accommodate volumetric expansion of active material. During delithiation, its reduced strength and enhanced flexibility facilitated volumetric contraction of active materials and maintained electrical and ionic contact. Thus, the dynamic flexibility in mechanical properties makes HOS-PFM a promising binder for high-energy density batteries.

Characterization of ballistic ion conductivity and long-range transport

Due to complicated interactions between ions and electrons within MEIC polymers,[24] it remains a challenge to accurately

measure their σ^+. Two LPSCl layers were utilized as an electronic blocking configuration to filter out electrons, allowing Li^+ to pass through HOS-PFM polymers for σ^+ measurement (Fig. S12). The high σ^+(~10^{-3} S cm^{-1})[25, 26] and wide operating temperature range of LPSCl made them suitable for characterizing the σ^+ of HOS-PFM from -20 °C to 70 °C. With either 0.32 g or 0.2 g LPSCl filters, both 100% Li^+-doped HOS-PFM exhibited a superior σ^+ at room temperature, approximately 10^{-4} to 10^{-3} S cm^{-1} (Fig. 2f; Fig. S13-S16; Tables S3,S4; Note S7).The ballistic ion transport within HOS-PFM followed Arrhenius temperature variation $\sigma \sim \exp(-E_o/kT)$, demonstrating solid-like transport mechanism.[5] In comparison, the pristine HOS-PFM samples lacked doped Li^+ content and thus featured poor σ^+, nearly three orders of magnitude lower than that observed in Li^+/HOS-PFM samples (Fig. 2f). The PFM possessed negligible Li^+ capacity (Fig. S4), thereby leading to low σ^+ at both undoped and doped conditions (Fig. S13).

By utilizing a tailor-designed sample preparation strategy (Fig. S17; Note S8), the crystallinity loss of Sn particles detected by X-ray diffraction (XRD) technique provided evidence of macroscopic transport Li^+, Na^+, K^+ within the HOS-PFM polymers (Note S9). After compressing Li metal, the PFM/Sn DLEs retained all major characteristic XRD peaks of Sn, including the two most distinctive peaks at 2θ values of 30.6° and 32.0° (Fig. 3a). However, the intensities of these peaks were slightly decreased, suggesting that partial crystalline Sn particles experienced an amorphous transition due to lithiation. In comparison, all characteristic peaks of Sn particles within HOS-PFM/Sn DLEs had completely disappeared, showing complete transformation of crystalline Sn particles into amorphous lithium tin (Li_xSn) compounds.[27-30] The lithiation process induced mechanical stress, volume expansion, and lattice expansion, leading to crystallinity loss of Sn nanoparticles. The complete reaction of Sn nanoparticles demonstrated the ability of Li^+ to travel through ~2 µm thick HOS-PFM layers in solid-state condition. In an attempt to acquire more validation, Sn(PFM) and Sn(HOS-PFM) single-layer composite electrodes underwent the same tests, and these electrodes exhibited similar XRD results (Fig. S18). Besides, their cross-sectional morphological evolution prior to and after Li metal compression (Fig. S19,S20) confirmed that the Sn particles within Sn(HOS-PFM) electrodes experienced complete reactions while only partial reaction occurred within the Sn (PFM) electrodes. In addition, after compressing Li metal, the Si/PFM and Si/HOS-PFM DLEs present similar XRD results to the Sn/PFM and Sn/HOS-PFM DLEs (Fig. S21). When replacing Li with Na or K metal, the XRD experiments showed the HOS-PFM featuring the capacity to transport Na^+ and K^+ across a macroscopic distance in a solid-state environment (Fig. S22-24; Note S10,S11), highlighting its potential applications for Na- and K-based energy storage devices.

When Li^+ ions pass through the HOS-PFM layers and react with Sn particles, it leads to ~300% volume expansion of Sn (Fig. 3b). Thereby, the morphological evolution of Sn particles can provide visual evidence to evaluate whether the HOS polymers possess the capability to transport Li^+.

The pristine HOS-PFM/Sn DLEs contained 2-µm thick HOS-PFM layer and isolated Sn particles (Fig. 3c; Fig. S25; Note S12). These two factors eliminated possible direct contact between Li and Sn during the compression and determined that Li^+ must travel through the HOS-PFM layers to reach Sn particles. After the compression, Sn nanoparticles (diameter ~100-300 nm) were converted into Li_xSn nanoparticles (diameter ~ 300 nm-1 µm), accompanied by nearly 300% volume expansion (Fig. 3d, Fig. S26). This observation agrees with theoretical volume expansion of Sn after lithiation. Owing to the volume expansion, the average interfacial distances among Sn nanoparticles was significantly reduced, and thus Sn nanoparticles were approaching closer to each other. This dimensional expansion of Sn particles provided visual evidence that a significant amount of Li^+ successfully diffused through the HOS-PFM layer. Additional experiments also revealed that Li^+ could effectively traverse HOS-PFM but not PFM (Fig. S27,S28, and Note S12). The rigid, densely packed, and well aligned conjugated backbones of HOS-PFM polymer possessed negligible polymer segmental motion. Therefore, we proposed that HOS-PFM polymers exhibit a unique ballistic ion transport mechanism, where Li^+ diffuses through the polymer matrix, counterbalanced by electrons on conjugated backbones. For comparison with other commonly used polymers, polyvinylidene fluoride (PVDF) and polyethylene oxide (PEO) were used to fabricate the PVDF/Sn and PEO/Sn DLEs. After compressing Li metal, the Sn particle sizes within both the PVDF/Sn and PEO/Sn DLEs remained unchanged (Fig. S29; Note S13).

Solid-state battery application

Designing a high-performance silicon-based ASSBs requires elevated levels of both electronic and ionic conduction, even in the presence of drastic volume changes of Si during battery cycling.[31, 32] Currently, poor σ^+ within electrode material is considered as a bottleneck restricting the high-energy-density silicon-based ASSBs. We engineered anode electrodes containing only HOS-PFM polymer (40 wt%) and Si particles (60 wt%), without any electronically or ionically conductive additives (Fig. 4a). The high mass composition of HOS-PFM polymer was intentionally designed to isolate the Si particles, providing additional evidence that Li^+ ions can transport through the HOS-PFM polymer. In addition, anode electrodes with a similar mass loading, composed of Si, PVDF, PEO, carbon black (CB) in weight ratio of 60:10:20:10, was fabricated for comparison. Although both have similar mass loadings (~1 mg/cm^2), the Si/PVDF/PEO/CB electrodes (~ 6 µm) are slightly thicker than the Si/HOS-PFM (~ 5µm) electrodes due to their higher porosity (Fig.4 a,b; Fig. S30,S31). PVDF functions as a binder. PEO combined with LiTFSI (molar ratio EO:Li=20:1) provides ionic conductivity. Carbon black offers electrical conductivity. The high performance of Si-based electrodes requires strong binding adhesion, ionic conductivity, and

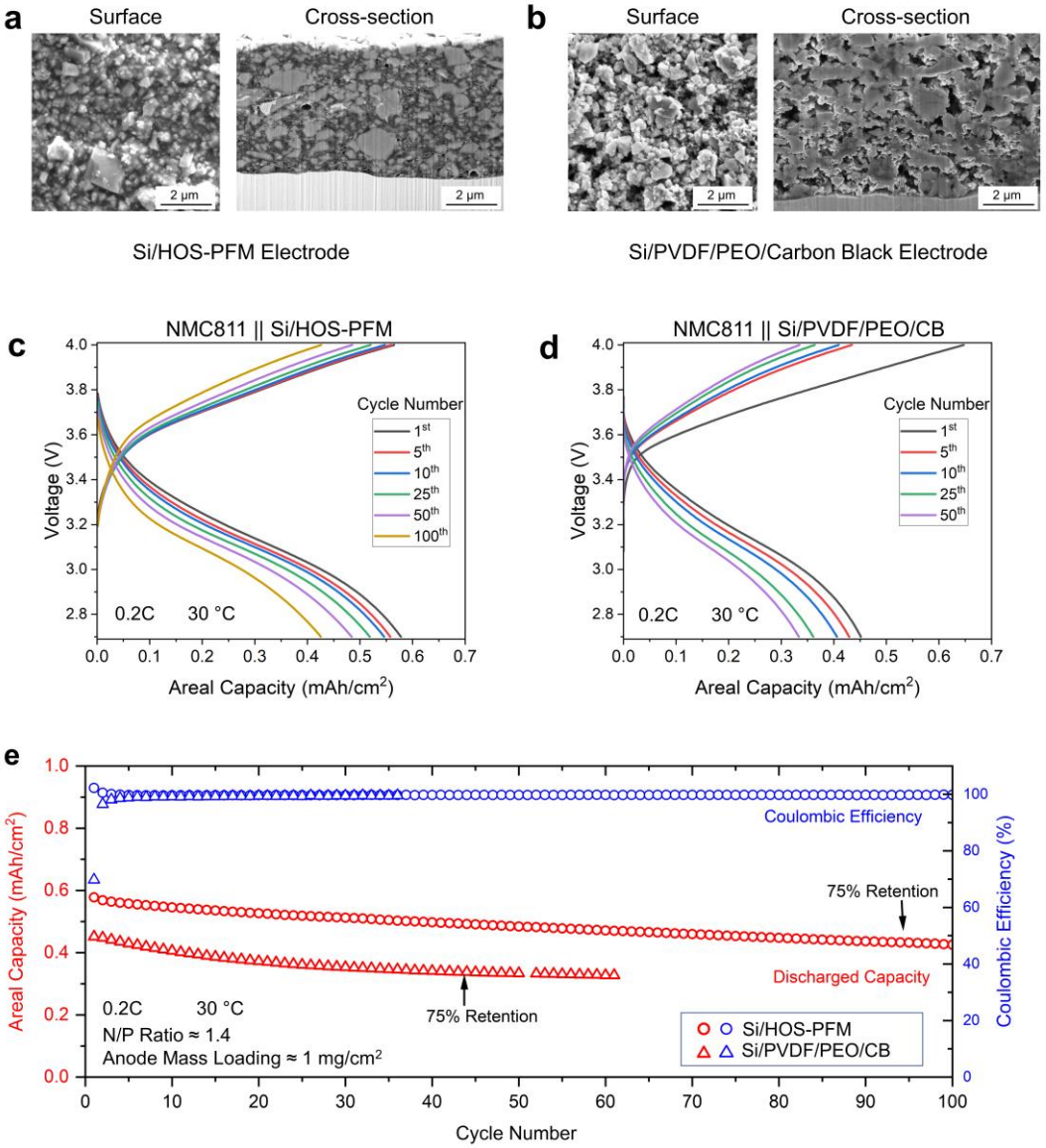

Fig. 4 Comparison of Si/HOS-PFM and conventional Si/PVDF/PEO/Carbon black (CB) electrodes with a similar mass loading. (a, b) Surface and cross-sectional SEM images of pristine (a) Si/HOS-PFM and (b) Si/PVDF/PEO/CB electrodes. (c, d) Voltage profiles of (c) Si/HOS-PFM and (d) Si/PVDF/PEO/CB electrodes over different cycles. These Si-based anodes, paired with NMC811 cathodes, were cycled at 0.2C and 30 °C. (e) Capacity retention of all-solid-state full cells based on the results from (c) and (d).

electrical conductivity. Therefore, the absence of PVDF, PEO, or carbon black can reduce battery performance under these experimental conditions.

The HOS-PFM polymers played the roles of electronic and ionic conductors, creating electronic and ionic pathways bridging active material Si with current collector and solid electrolyte separator, respectively. Moreover, the HOS-PFM functioned as polymer binders, which not only maintained structural integrity and accommodated drastic volume change of Si but also ensured good electrical and ionic contact with Si during battery cycling. The combined MEIC and adhesion attributes of HOS-PFM contributed to remarkable full-cell ASSB performance. In addition, the HOS-PFM exhibited a stable interface with the solid electrolyte LPSCl (Fig. S32, S33). The Si/HOS-PFM full cells preserved 75% of their capacity after 94 cycles at 0.2 C rate (Fig. 4c, 4e; Fig. S34; Note S14). In comparison, the full cells with Si/PVDF/PEO/CB anodes retained 75% of their capacity after only 44 cycles (Fig. 4d, 4e). The HOS-PFM polymers extended the cycle life of full cells by 114%, outperforming the combination of PVDF, PEO, and carbon black. Additionally, the ASSB performance demonstrated the feasibility of leveraging ballistic Li^+ transport in practical applications, pioneering a new HOS polymer research field in solid-state energy.

Conclusions

In conclusion, we report a unique ballistic ion transport, where Li^+ diffuse through the polymer matrix, counterbalanced by electrons on the conjugated backbone. This ballistic ion transport exhibits the capability to transport Li^+ over macroscopic distance in solid-state environments. Additionally, it possesses several advantages that are inaccessible through conventional ion transport by polymer segmental dynamics, including σ^+ in the approximate range of 10^{-4} to 10^{-3} S cm^{-1} across a broad temperature range and overcoming the tradeoff between σ^+ and mechanical robustness. The ballistic ion transport concept provides motivation and an innovative molecular design principle for engineering a class of HOS polymers for energy storage, energy conversion, and organic electronics that require elevated electronic and ionic conductivity.

Experimental

Material Availability

Sn nanoparticles (99% purity, diameter ~100-300 nm) were purchased from Sigma-Aldrich. Poly(9,9-dioctylfluorene-co-fluorenone-comethylbenzoicester) (PFM) was synthesized based on previous protocol.[17, 18] Lithium (Li) metal with thicknesses of 25 µm and 100 µm was obtained from Applied Materials and MSE Supplies LLC, respectively. Sodium cubes and potassium trunks were purchased from Sigma Aldrich.

Electrode Fabrication

Sn(PFM) and Sn(HOS-PFM) Single Layer Electrode Preparation: 0.294 g of PFM was dissolved in 3.26 mL of chlorobenzene to prepare a 7.5 wt% PFM solution in a PTFE container. The container was sealed with a cap to avoid solvent evaporation and left for at least 12 hours to ensure complete dissolution. Subsequently, around 0.294g of Sn particles were transferred into the PFM solution to prepare a mixed Sn and PFM slurry with a weight ratio of 1:1. The slurry underwent a series of mixing cycles, comprising 5 minutes of ball milling and then followed by a resting period of 20 minutes, repeated three times.

A doctor blade with a height of 200 µm was used to apply a uniform slurry film on a 16-µm thick copper foil surface. The slurry film was allowed to evaporate all solvent over a minimum period of 2 hours, followed by overnight vacuum drying at 80 °C in a glove box chamber. The resultant sample was named the Sn(PFM) single-layer composite electrode. Subsequently, the Sn(PFM) single-layer composite electrode samples underwent a heat treatment at 500 °C for 10 minutes using a tube furnace with a heating ramp rate of 4 °C/min. During thermal processing, the PFM underwent thermal decomposition and was transformed into HOS-PFM polymer. The resulting sample was referred to as the Sn(HOS-PFM) single-layer composite electrode.

PFM/Sn and HOS-PFM/Sn Double Layer Electrode (DLE) Preparation: An appropriate amount of PFM polymer was dissolved in chlorobenzene to prepare 5 wt% PFM viscous solution. The double layer electrodes were prepared by applying another PFM or HOS-PFM on the top of the Sn(HOS-PFM) single-layer composite electrodes. A doctor blade with a height of 200 µm was utilized to apply a homogenous film on the surface of the Sn(HOS-PFM) single-layer composite electrodes. Following vacuum drying overnight, the resultant double layer electrode sample was named PFM/Sn double-layered electrodes (DLEs). Subsequently, the PFM/Sn DLEs were processed with heating treatment at 500 °C to obtain the HOS-PFM/Sn DLEs, in which the PFM polymer on the upper layer was transformed into HOS-PFM.

Lithiation via Solid-State Redox Doping

The Sn(PFM) and Sn(HOS-PFM) single-layer composite electrodes were cut into many square pieces, each measuring 1 cm in width. Similarly, Li foil with a thickness of 100 µm were prepared into square pieces with dimension slightly larger than 1 cm to fully cover the surface area of these single layer composite electrodes. The Li metal square pieces were positioned atop the Sn(PFM) and Sn(HOS-PFM) single-layer composite electrodes. Subsequently, the assemblies, which comprised the Sn-based single-layer composite electrodes and Li metal square pieces, were interposed between two spacers. Then, those assemblies were subjected to a hydraulic press with a force of 1 ton, employed for compression for one day.

Similar approaches were applied to prepare double layer electrode samples. The PFM/Sn DLEs and HOS-PFM/Sn DLEs were cut into square pieces, each featuring 1 cm in width. In contrast to those single layer composite electrodes, these double-layer electrodes featured an additional layer of either PFM or HOS-PFM layer on their top surface, leading to increased overall material thickness. Therefore, the compression durations of double layer electrode samples for Li metal, Na metal, and K metal were extended to 3, 12, and 5 days, respectively, in order to achieve completed reaction of Sn particles in the HOS-PFM/Sn DLEs.

FIB-SEM Experiments

The Sn and PFM slurry was prepared by following the same method described in the preceding section, 'Electrode Fabrication'. The slurry was coated with a doctor blade with a height of 100 µm on a 4.5 µm thick copper foil. The reason for utilizing a lower doctor blade height and a thinner copper foil is to facilitate the ion milling process by FIB-SEM. After following the same thermal treatment at 500 °C, the resultant Sn(HOS-PFM) single layer treated with the same method outlined in the previous section, 'Electrode Fabrication', to obtain Sn(HOS-PFM) DLE samples for FIB-SEM experiments. These samples later were lithiated by the protocols described in the previous section, 'Lithiation via Solid-State Redox Doping'. The FIB-SEM ion milling technique typically has a limited depth of around 15-30 µm owing to material redeposition. Therefore, this sample preparation method enabled the FIB-SEM ion milling from copper foil side and avoid the ultra-thick Li metal foil.

The FIB-SEM experiments were performed at the National Center for Electron Microscopy (NCEM), Laurence Berkeley National Laboratory. The samples underwent initial ion milling utilizing FIB-SEM at 30 kV and 9 nA to acquire rough cross-sections. Subsequently, those cross-sections were further

polished using FIB-SEM at 30 kV and 0.72 nA to obtain a smooth and pristine surface. Compared to a traditional ion-milling machine, using FIB-SEM machine to prepare cross-sections provides the advantage of avoiding the sample transport in air.

Soft X-ray Absorption Spectroscopy (sXAS)

The sXAS spectra in partial fluorescence yield (PFY) mode are extracted from high-efficiency mapping of resonant inelastic x-ray scattering (RIXS) at beamline 8.0.1.1 of Advanced Light Source (Lawrence Berkeley National Laboratory). The ht-RIXS detector in the beamline was used to collect the spectra, and partial fluorescence yield was extracted by integrating the intensity across emission energy range with the range of carbon *K*-edge (Fig. S9). In order to eliminate the radiation damage effects, we have purposely changed several experimental parameters: (i) the samples are cooled down by liquid N_2 to about 80 K; (ii) the sample was kept moving ± 0.1 mm throughout the data collection; and (iii) the beam was defocused to minimize the area disposure dose. C=C π* excitation of highly ordered pyrolytic graphite (HOPG) was measured set to 285 eV for calibrating the excitation energies.

Solid-state NMR Characterization

^{1}H and ^{13}C solid-state NMR (ssNMR) spectra were recorded at B_0= 9.4 T (400.1 MHz for ^{1}H) using a Bruker BioSpin spectrometer equipped with an AVANCE NEO console and a 3.2 mm double resonance HX magic angle spinning (MAS) probe tune to both ^{1}H (400.1 MHz) and ^{13}C (100.6 MHz). Before NMR experiments, PFM and HOS PFM were pulverized into fine powder following different procedures due to their distinct bulk properties. PFM was first cryogenically frozen using liquid nitrogen to reach a brittle state, then ground using a mortar and pestle. HOS PFM was directly crushed into power with a mortar and pestle without any other step needed. For NMR experiments, powdered samples of PFM and HOS PFM were loaded in thin wall 3.2mm zirconia rotors and closed using Vespel® caps. Samples were spun at the magic angle at ν_R = 20 kHz using dry nitrogen. ^{1}H and ^{13}C chemical shift were referenced with respect to tetramethylsilane using the CH_2 resonance of adamantane as a secondary external reference at $\delta_{iso}(^{13}C)$= 38.48 ppm and $\delta_{iso}(^1H)$= 1.8 ppm.

^{1}H ssNMR spectra were obtained using a rotor synchronized spin-echo sequence (90° – τ_R – 180° – τ_R – AQ) with a 90° radio frequency (RF) pulse of 1.96 µs equivalent to an RF-field of 127.55 kHz. For quantitative ^{1}H spin-echo spectra (τ_R = 1 rotor period), a total of 16 (PFM) or 32 (HOS PFM) transients were average using a repetition time of 5 s which was long enough to reach full relaxation of all ^{1}H signals in both samples.

^{13}C ssNMR spectra were obtained using a ^{1}H→^{13}C cross-polarization (CP) transfer under MAS (CPMAS). The CPMAS experiments used a contact time of τ_{CP} = 2.0 ms, during which a constant RF-field equal to 80.4 kHz was applied on the ^{13}C, while the ^{1}H RF-field amplitude was linearly ramped from 90.4 to 100.4 kHz. During ^{13}C acquisition, high-power ^{1}H decoupling was applied using the SPINAL-64 (Small Phase Incremental Alternation with 64 steps) decoupling scheme with an RF-field amplitude set to 110.4 kHz.[33] A total of 512 and 2048 transients were averaged with a repetition time of 3 s resulting in experimental times of 26 min and 1 h 43 min for PFM and HOS PFM, respectively.

All solid-state NMR data were processed using Bruker TopSpin 4.2.0 and DMfit software.[34]

Author contributions

D.L. and G.L. conceptualized this study and designed the experiments. D.L. performed and assisted all experiments. D.L. designed and performed transport experiments. F.C. designed EIS analysis experiments. F.C., D.L. and F. A. performed EIS analysis. S.T. and Y.T.C designed and measured the mechanical properties. H.S. and A.M. designed and performed the 4-D STEM experiments. G.Lee and W.Y. designed and performed the sXAS measurement. F.A. and D.L. performed solid-state battery experiments. R.G. and D.L. designed and performed the ssNMR measurement. X.J. and E.M. performed ICP experiments. D.L. and G.L. completed the initial draft of this manuscript. All authors provided comments and revisions on the manuscript.

Conflicts of interest

The authors declare no competing interests.

Data availability

All data supporting this article are included in the manuscript and supplementary information. Correspondence and material requests should be addressed to Gao Liu.

Acknowledgements

This work was supported by the U.S. Department of Energy, Vehicle Technologies Office, through the Advanced Battery Materials Research Program, the Solid-State Battery Program, and the I4-Lab Program, and by Lawrence Berkeley National Laboratory through its Directed Research and Development (LDRD) program. Focused ion beam scanning electron microscopy (FIB-SEM) and 4D scanning transmission electron microscopy (4D STEM) experiments were conducted at the National Center for Electron Microscopy (NCEM) and The Molecular Foundry (TMF), while soft X-ray experiments were performed at BL8.0.1 of the Advanced Light Source (ALS), all U.S. Department of Energy Office of Science User Facilities located at Lawrence Berkeley National Laboratory, under contract no. DE-AC02-05CH11231. The Pines Magnetic Resonance Center's Core NMR Facility (PMRC Core) used in this work is supported by the National Science Foundation under Grant No. 2018784. The authors thank Dr. Hasan Celik for spectroscopic assistance and Dr. Tianyu Zhu and Dr. Vincent Battaglia for helpful discussions.

References

1. D. E. Fenton, J. M. Parker and P. V. Wright, *Polymer*, 1973, **14**, 589.
2. P. V. Wright, *British Polymer Journal*, 1975, **7**, 319-327.
3. Z. Xue, D. He and X. Xie, *Journal of Materials Chemistry A*, 2015, **3**, 19218-19253.
4. Z. Song, F. Chen, M. Martinez-Ibañez, W. Feng, M. Forsyth, Z. Zhou, M. Armand and H. Zhang, *Nature Communications*, 2023, **14**, 4884.
5. V. Bocharova and A. P. Sokolov, *Macromolecules*, 2020, **53**, 4141-4157.
6. L. Long, S. Wang, M. Xiao and Y. Meng, *Journal of Materials Chemistry A*, 2016, **4**, 10038-10069.
7. K. Xu, *Chemical Reviews*, 2014, **114**, 11503-11618.
8. D. T. Hallinan Jr and N. P. Balsara, *Annual Review of Materials Research*, 2013, **43**, 503-525.
9. B. D. Paulsen, K. Tybrandt, E. Stavrinidou and J. Rivnay, *Nature Materials*, 2020, **19**, 13-26.
10. J. Jang, J. Ha and J. Cho, *Advanced Materials*, 2007, **19**, 1772-1775.
11. S. van Reenen, T. Akatsuka, D. Tordera, M. Kemerink and H. J. Bolink, *Journal of the American Chemical Society*, 2013, **135**, 886-891.
12. H. Erothu, J. Kolomanska, P. Johnston, S. Schumann, D. Deribew, D. T. W. Toolan, A. Gregori, C. Dagron-Lartigau, G. Portale, W. Bras, T. Arnold, A. Distler, R. C. Hiorns, P. Mokarian-Tabari, T. W. Collins, J. R. Howse and P. D. Topham, *Macromolecules*, 2015, **48**, 2107-2117.
13. H. Jiang, P. Taranekar, J. R. Reynolds and K. S. Schanze, *Angewandte Chemie International Edition*, 2009, **48**, 4300-4316.
14. A. Giovannitti, C. B. Nielsen, D.-T. Sbircea, S. Inal, M. Donahue, M. R. Niazi, D. A. Hanifi, A. Amassian, G. G. Malliaras, J. Rivnay and I. McCulloch, *Nature Communications*, 2016, **7**, 13066.
15. S. T. Keene, V. Gueskine, M. Berggren, G. G. Malliaras, K. Tybrandt and I. Zozoulenko, *Physical Chemistry Chemical Physics*, 2022, **24**, 19144-19163.
16. J. Rivnay, S. Inal, B. A. Collins, M. Sessolo, E. Stavrinidou, X. Strakosas, C. Tassone, D. M. Delongchamp and G. G. Malliaras, *Nature Communications*, 2016, **7**, 11287.
17. G. Liu, S. Xun, N. Vukmirovic, X. Song, P. Olalde‐Velasco, H. Zheng, V. S. Battaglia, L. Wang and W. Yang, *Advanced Materials*, 2011, **23**, 4679-4683.
18. M. Wu, X. Xiao, N. Vukmirovic, S. Xun, P. K. Das, X. Song, P. Olalde-Velasco, D. Wang, A. Z. Weber and L.-W. Wang, *Journal of the American Chemical Society*, 2013, **135**, 12048-12056.
19. T. Zhu, H. Sternlicht, Y. Ha, C. Fang, D. Liu, B. H. Savitzky, X. Zhao, Y. Lu, Y. Fu, C. Ophus, C. Zhu, W. Yang, A. M. Minor and G. Liu, *Nature Energy*, 2023, 1-9.
20. U. Sternberg, R. Witter, I. Kuprov, J. M. Lamley, A. Oss, J. R. Lewandowski and A. Samoson, *Journal of Magnetic Resonance*, 2018, **291**, 32-39.
21. R. Zhang, K. H. Mroue and A. Ramamoorthy, *Accounts of chemical research*, 2017, **50**, 1105-1113.
22. Y. Nishiyama, G. Hou, V. Agarwal, Y. Su and A. Ramamoorthy, *Chemical reviews*, 2022, **123**, 918-988.
23. H. W. Spiess, *Macromolecular Chemistry and Physics*, 2003, **204**, 340-346.
24. M. J. Wang, J. B. Wolfenstine and J. Sakamoto, *Advanced Functional Materials*, 2020, **30**, 1909140.
25. C. Yu, S. Ganapathy, J. Hageman, L. van Eijck, E. R. H. van Eck, L. Zhang, T. Schwietert, S. Basak, E. M. Kelder and M. Wagemaker, *ACS Applied Materials & Interfaces*, 2018, **10**, 33296-33306.
26. C. Yu, L. van Eijck, S. Ganapathy and M. Wagemaker, *Electrochimica Acta*, 2016, **215**, 93-99.
27. D. Larcher, S. Beattie, M. Morcrette, K. Edstroem, J.-C. Jumas and J.-M. Tarascon, *Journal of Materials Chemistry*, 2007, **17**, 3759-3772.
28. C.-Y. Chou, H. Kim and G. S. Hwang, *The Journal of Physical Chemistry C*, 2011, **115**, 20018-20026.
29. P. Limthongkul, Y.-I. Jang, N. J. Dudney and Y.-M. Chiang, *Acta Materialia*, 2003, **51**, 1103-1113.
30. S. Xun, X. Song, V. Battaglia and G. Liu, *Journal of the Electrochemical Society*, 2013, **160**, A849.
31. I. Kovalenko, B. Zdyrko, A. Magasinski, B. Hertzberg, Z. Milicev, R. Burtovyy, I. Luzinov and G. Yushin, *Science*, 2011, **334**, 75-79.
32. D. H. Tan, Y.-T. Chen, H. Yang, W. Bao, B. Sreenarayanan, J.-M. Doux, W. Li, B. Lu, S.-Y. Ham and B. Sayahpour, *Science*, 2021, **373**, 1494-1499.
33. B. M. Fung, A. K. Khitrin and K. Ermolaev, *Journal of Magnetic Resonance*, 2000, **142**, 97-101.
34. D. Massiot, F. Fayon, M. Capron, I. King, S. Le Calvé, B. Alonso, J. O. Durand, B. Bujoli, Z. Gan and G. Hoatson, *Magnetic Resonance in Chemistry*, 2002, **40**, 70-76.

Data availability

All data supporting this article are included in the manuscript and supplementary information. Correspondence and material requests should be addressed to Gao Liu.